

Heterogeneous & Homogeneous & Bio- & Nano-

CHEM**CAT**CHEM

CATALYSIS

Accepted Article

Title: Oxidative esterification of methacrolein to methyl methacrylate over gold nanoparticles on hydroxyapatite

Authors: Jun Gao, Guoli Fan, Lan Yang, Xinzhong Cao, Peng Zhang, and Feng Li

This manuscript has been accepted after peer review and appears as an Accepted Article online prior to editing, proofing, and formal publication of the final Version of Record (VoR). This work is currently citable by using the Digital Object Identifier (DOI) given below. The VoR will be published online in Early View as soon as possible and may be different to this Accepted Article as a result of editing. Readers should obtain the VoR from the journal website shown below when it is published to ensure accuracy of information. The authors are responsible for the content of this Accepted Article.

To be cited as: *ChemCatChem* 10.1002/cctc.201601560

Link to VoR: <http://dx.doi.org/10.1002/cctc.201601560>

Oxidative esterification of methacrolein to methyl methacrylate over gold nanoparticles on hydroxyapatite

Jun Gao,^a Guoli Fan,^a Lan Yang,^a Xinzhong Cao,^c Peng Zhang,^c Feng Li^{a,b*}

Presently, the catalytic production of methyl methacrylate through direct oxidative esterification of methacrolein is important in terms of green chemistry and sustainable development. In the present work, three needle-like, lamella-like, and rod-like hydroxyapatites supported Au nanoparticles were synthesized. It was demonstrated that needle-like hydroxyapatite could facilitate the higher dispersion of Au species, owing to higher specific surface area, and that the stronger interaction between Au NPs and the support resulted in the formation of more surface defects, due to the existence of partially encapsulated Au particles by the needle-like hydroxyapatite. Meanwhile, surface defects were found to be closely related to the generation of strong basic sites. Compared with other two ones, needle-like hydroxyapatite supported catalyst

with a larger amount of surface acid-base sites exhibited much higher catalytic activity and selectivity to methyl methacrylate in direct oxidative esterification of methacrolein with methanol under mild reaction conditions (i.e., ambient pressure, low reaction temperature of 70 °C, and low methanol/aldehyde ratio of 8:1). Superior catalytic performance of needle-like hydroxyapatite supported catalyst was attributable to a cooperative effect between abundant acid-base sites for the preferential chemisorption of methacrolein and highly dispersed active Au species for the favorable formation of β -hydride and oxygen activation. The present findings open a new and promising route for the practical production of methyl methacrylate using high-performance HAP-supported metal catalyst systems.

Introduction

Methyl methacrylate (MMA) is an important and widely used polymer monomer or chemical intermediate for the production of acrylic plastics (e.g. polymethyl methacrylate), paints, adhesives, and other important fine chemicals.^[1] For this, the production of MMA can be performed by several methods, such as partial oxidation/coupling of ethylene, propylene or isobutene and acetone cyanohydrin (ACH) method.^[2-5] Among them, the partial oxidation/coupling of ethylene has an obvious shortcoming of low conversion rate, and the isobutene oxidation goes through a complicated multi-step route including the oxidation of isobutene to methacrylic acid and the following conversion of methacrylic acid to MMA. Currently, the production of MMA has been carried out commercially by the traditional ACh method. This unsustainable method, however, has several drawbacks including long technological route, high cost, strong corrosion of hydrocyanic acid raw material, and serious environmental

pollution of sulfuric acid used.^[2] Therefore, developing a green approach for the production of MMA is of far-reaching significance. As an ideal alternative, direct oxidative esterification of methacrolein (MA) with methanol to produce MMA using molecular oxygen is attracting considerable attention,^[6] because it is an environmentally friendly, greatly simplified and cost-effective production process with good atom economy in comparison to other production processes.

Recently, many efforts have been made to oxidative esterification of MA by using heterogeneous Pd-based catalysts.^[6-9] Specially, the addition of second metal Pb can further improve the catalytic activity,^[8,9] regardless of low selectivity to MMA (< 90%). In addition, for the oxidative esterification of aldehydes or alcohols, Au-based catalysts also exhibit high selectivity to esters.^[10-13] However, in most cases, harsh reaction conditions,^[11-13] such as the use of a large excess of methanol, need of basic additives in the reaction mixture to inhibit the generation of by-products, high energy consumption, and long reaction time, greatly limit their practical applications. Therefore, designing new highly efficient catalyst systems for the oxidative esterification of MA has been an important and urgent task in terms of green chemistry and sustainable development.

Currently, supported gold-based catalysts have received numerous attention due to their unique catalytic properties in many important types of chemical reactions.^[14-19] However, these catalysts suffer from problems, such as easy agglomeration of gold nanoparticles (NPs) and thus rapid decline in the activity during reactions. It is well known that for supported metal catalysts, the interactions between metals and supports can greatly affect electronic structures of active species and thus significantly govern their catalytic performances,^[20-22] besides the size and geometry of metal particles and the acid–base property of supports. Specially, it was reported that strong metal-support interactions

[a] J. Gao, Dr. G. Fan, Prof. L. Yang, Prof. F. Li
State Key Laboratory of Chemical Resource Engineering
Beijing University of Chemical Technology
Beijing, 100029, P. R. China.
E-mail: lifeng@mail.buct.edu.cn; Fax: +8610-64425385;
Tel.: +8610-64451226

[b] Prof. F. Li
Beijing Advanced Innovation Center for Soft Matter Science and
Engineering, Beijing 100029, China.

[c] Dr. X. Cao, P. Zhang
Key Laboratory of Nuclear Radiation and Nuclear Energy
Technology, Institute of High Energy Physics, Chinese
Academy of Sciences, Beijing 100049, P. R. China

Supporting information for this article is available on the WWW
under <http://dx.doi.org/10.1002/cctc.xxxxx>.

(SMSI) could form if metals were encapsulated by suitable supports.^[23,24] In this regard, Zhang et. al found that hydroxyapatite (HAP) could strongly interact with Au NPs,^[24] thereby facilitating the immobilization and dispersion of active components and inhibiting the growth of metal NPs.

Commonly, HAP with the formula $\text{Ca}_{10}(\text{PO}_4)_6(\text{OH})_2$, which belongs to the hexagonal cylinder crystal structure,^[25] is widely used as green, substrate-tolerant, nearly water-insoluble, and easy to recover catalyst support with excellent ion exchange/adsorption ability and tunable surface acid-base property.^[26-33] Especially, many base-catalyzed reactions,^[34-36] as well as Guerbet reaction for the production of n-butanol from ethanol,^[37-40] can be efficiently promoted by HAP-based catalyst systems. In addition, the lattice oxygen in the structure of HAP may improve the oxidation activity of supported metal catalysts.^[41] Thus, it is probable that reasonably regulating the microstructure and surface acid-base property of HAP supports can greatly enhance catalytic performances of corresponding catalysts.

Taking into account the above scenarios, in this work, we first synthesize supported Au nanocatalysts based on three different types of needle-like, lamellar-like and rod-like HAP supports. The results demonstrate that small and uniform Au NPs can be tightly anchored onto the surface of HAP supports and even partially embedded into supports, thereby resulting in the SMSI and the formation of a large number of surface defects. The effects of the microstructures of HAP supports on metal-support interactions, surface acid-base properties, surface defects, electronic structures of Au species, and catalytic performance of catalysts are studied systemically. Compared with lamella-like and rod-like HPA supported ones, needle-like HAP supported Au catalyst displays much higher catalytic performance in the oxidative esterification of MA in terms of both the activity and the MMA selectivity under mild reaction conditions (i.e., low methanol/MA ratio, low reaction temperature and ambient pressure). High catalytic efficiency is attributed to a cooperative effect between abundant surface acid-base sites and highly dispersed active Au species, thereby facilitating the chemisorption of reactants and the following activation.

Results and Discussion

Structural characterization

As shown in Figure 1, all of HAP-supported Au samples present characteristic diffractions of (002), (102), (210), (211), (112), (300), (202), (310), (222), (213) crystal planes of hexagonal HAP phase (JCPDS No. 73-0293), respectively. It is worth noting that an impure CaHPO_4 phase (JCPDS No. 70-0360) is detected in the Au/R-HAP. In addition, due to the fact that the positions for the (104) plane of two different crystalline CaCO_3 phases (JCPDS No. 72-1652 and JCPDS No. 86-2343) partially coincide with that for the (210) diffraction of hydroxyapatite, the relatively high intensity of the (210) diffraction line demonstrates the presence of CaCO_3 impurity in the Au/R-HAP. Two Ca-containing impurities possibly originate from the weak basicity in the synthesis solution and the affinity

of HAP for carbonatation. In all cases, no characteristic diffractions related to metallic Au phase are observed, mirroring the highly dispersive nature of Au species on supports, as well as the low actual Au content (Table 1).

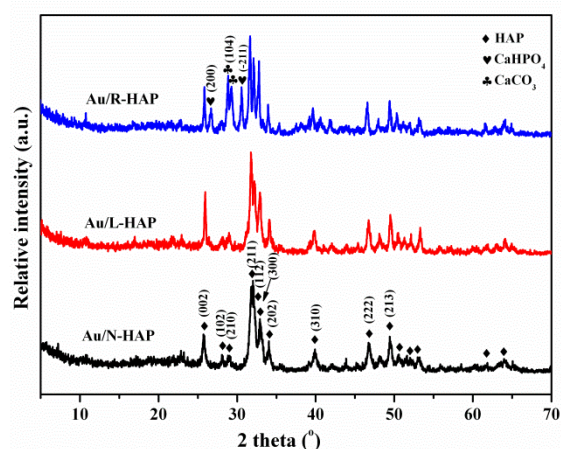


Figure 1. XRD patterns of different HAP-supported Au samples.

Figure 2 shows the morphologies of three HAP supports. Nanometric N-HAP crystals present an oriented array structure of several needles with a width of 100–150 nm (Figure 2a-c). As shown in Figure 2d-f, the morphology of nano lamellas with a width of 150–200 nm is formed in the L-HAP. Such structure may be constructed through a parallel assembly of needle-like crystals elongated in the *c* direction, as proved by relatively sharpened diffractions compared with those for N-HAP (Figure 1). Long and uniform rod-like fibers with the diameter of 100–150 nm elongated along the *c* axis can be found in the case of R-HAP (Figure 2g-i). Here, the formation of different morphologies of needle-like, lamella-like and rod-like HAPs should mainly originate from different basic conditions and ion concentrations applied in synthesis solutions,^[42] thus leading to different precipitation routes and growth modes of HAP crystals.

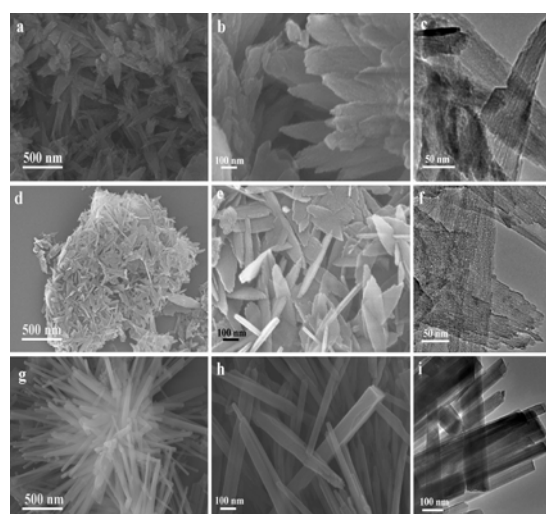


Figure 2. SEM and TEM images of hydroxyapatite supports with different morphologies: N-HAP (a,b,c), L-HAP(d,e,f) and R-HAP (g,h,i).

Figure 3 shows TEM and HRTEM images of different supported Au samples. In each case, a large number of small black NPs with narrow particle distributions are well dispersed on the HAP support. However, smaller Au clusters or atomically dispersed mono-layer Au species cannot be found regardless of supports, mainly due to the limitation of preparation method, as well as relatively high Au loading of about 1.8 wt.% (Table 1). Typically, the lattice fringes of single particle clearly indicate an exposed (200)

plane of Au⁰ NPs with an interplanar spacing of about 0.203 nm in the case of Au/R-HAP, while the lattice fringes related to (202) plane of hexagonal HAP phase with an interplanar spacing of about 0.262 nm are clearly observed. According to the size distributions of Au NPs, the average diameter of Au NPs on N-HAP (2.60 nm) and L-HAP (2.40 nm) are smaller than that on the R-HAP (4.55 nm), in spite of their identical Au loadings.

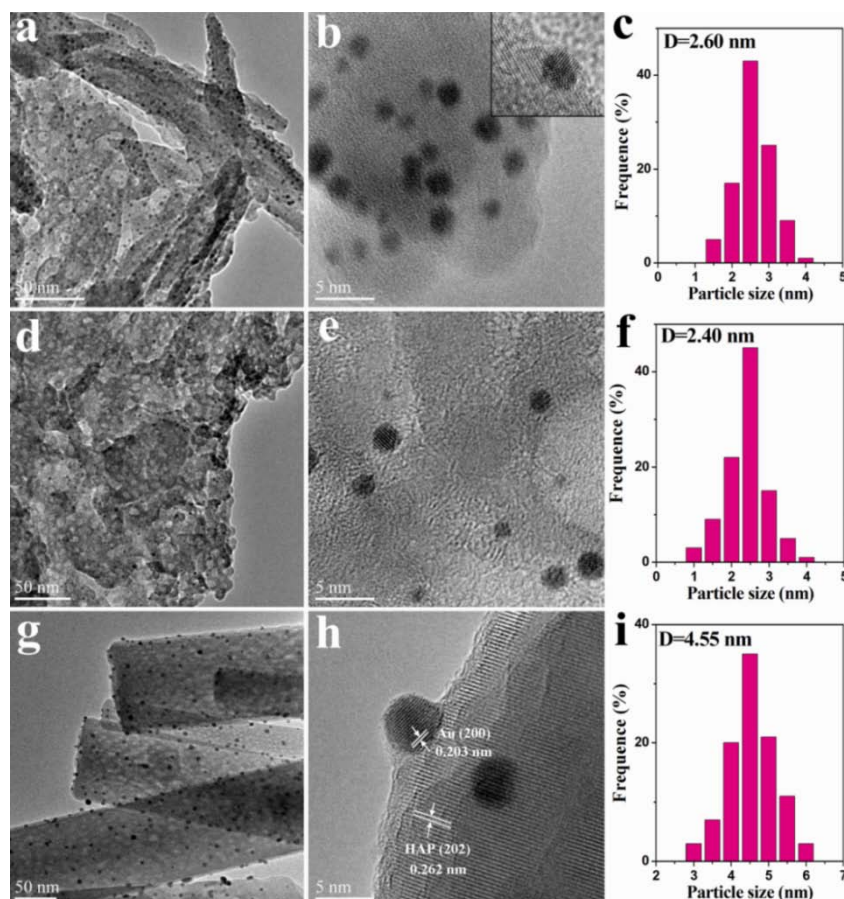


Figure 3. TEM images, HRTEM images and particle size distributions of Au/N-HAP (a,b,c), Au/L-HAP (d,e,f) and Au/R-HAP (g,h,i) samples. The inset in (b) shows the HRTEM image of a single particle on the Au/N-HAP.

Samples	Au ^[a] (wt %)	Ca/P ^[a] molar ratio	Dis ^[b] (%)	D _{TEM} ^[c] (nm)	S _{BET} ^[d] (m ² /g)	Au ^{δ+} /(Au ⁰ +Au ^{δ+}) ^[e] molar ratio	Specific acidity ^[f] (mmol/g)	Specific basicity ^[h] (mmol/g)
Au/N-HAP	1.82	1.43	32.3	2.60	84	0.36	0.351 (0.60) ^[g]	0.753 (0.328) ^[i]
Au/L-HAP	1.73	1.55	27.6	2.40	53	0.42	0.342 (0.48)	0.456 (0.187)
Au/R-HAP	1.75	1.58	26.0	4.55	14	0.49	0.280 (0.39)	0.356 (0.104)

[a] Analyzed by ICP-AES. [b] Au dispersion degree by CO pulse chemisorption. [c] Average particle size of Au NPs based on by TEM analysis. [d] BET specific surface areas. [e] Calculated based on XPS of Au 4f core levels. [f] The amount of total acid sites determined by NH₃-TPD. [g] The proportion of strong and super strong acid sites in the total amount of acid sites. [h] The amount of total base sites determined by CO₂-TPD. [i] The amount of strong and super strong base sites determined by CO₂-TPD.

The Cs-STEM is an excellent technique to precisely observe the microscopic structure and morphology. Thus, Cs-STEM images of Au NPs on different HAP supports were examined (Figure 4). It is interesting to note that for Au/N-HAP sample, some Au NPs are partially encapsulated by the N-HAP

support to a large extent (Figure 4a,b), forming an embedded structure of Au NPs with a large interface between Au NPs and the support. The above phenomenon implies the formation of SMSI. Similar result also is observed for Au/L-HAP with partially encapsulated Au NPs by the L-HAP and small

exposed surface of Au NPs (Figure 4c,d); however, embedded structure of Au NPs in the Au/R-HAP is not as pronounced as those in Au/N-HAP and Au/L-HAP (Figure 4e, f), as evidenced by a smaller interface between Au NPs and the support. Moreover, in the case of Au/N-HAP, Au NPs clearly show the distortion of lattice fringes, i.e., dislocation and rugged steps, indicative of the existence of more surface defects. Such surface defects on Au NPs can be formed by the structural reconstruction of the HAP support. It is well accepted that surface defects on metal particles are thought to have a crucial impact on the adsorption and activation of reactant molecules, probably responsible for the excellent catalytic performance in some heterogeneous catalytic reactions in a way.^[43]

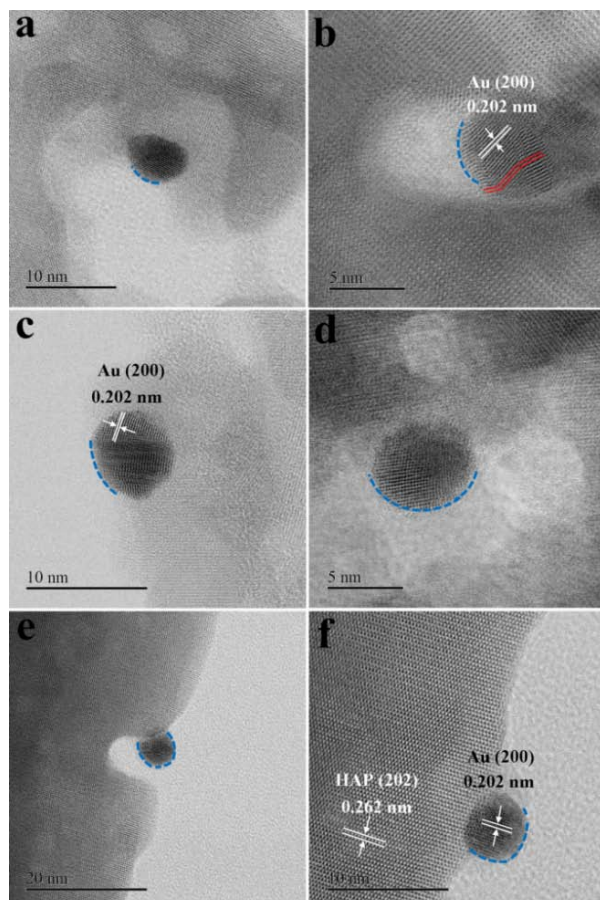


Figure 4. Cs-STEM images of Au/N-HAP (a,b), Au/L-HAP (c,d) and Au/R-HAP (e,f) samples, showing clear interface between Au NPs and supports. Images are colored in order to highlight the uncovered surface of Au NPs (blue broken lines) and some surface defects of Au NPs (red polylines).

Table 2 Positron lifetimes and relative intensities of different components for supported Au samples					
Samples	τ_1 [a] (ns)	τ_2 [a] (ns)	τ_3 [a] (ns)	τ_4 [a] (ns)	I_2/I_1 [b]
Au/N-HAP	0.175(40.4)	0.360(53.5)	1.51(4.2)	5.75(1.9)	1.32
Au/L-HAP	0.160(47.9)	0.325(47.2)	1.46(3.5)	5.69(1.4)	0.99
Au/R-HAP	0.171(47.9)	0.367(46.3)	1.72(4.4)	5.35(1.4)	0.97

[a] Values in parentheses are proportions of different components. [b] Relative intensity ratio of T2 component to T1 component.

Positron annihilation spectroscopy (PAS) is a powerful tool for detecting different types and relative densities of defects in solids.^[44] Table 2 shows four kinds of positron lifetime components (τ_1 , τ_2 , τ_3 and τ_4) and their relative intensities for supported Au samples. Among them, the component of the longest life (τ_4) is assigned to inter-crystallite spaces, while the third component (τ_3) is related to defects inside the crystallites or to positronium-surface bound state.^[45,46] The component of the shortest life (τ_1) with the similar τ_1 values for three samples is associated with small size bulk defects of particles (e.g. monovacancies),^[47,48] while the second component (τ_2) is generally caused by large size defects located on the surface boundary and interface of particles.^[49,50] Further, the higher relative intensity ratio of T2 component to T1 component for Au/N-HAP than those for other two supported samples apparently reflects that Au/N-HAP possesses a higher concentration of surface defects, well consistent with the Cs-STEM results. Accordingly, it is assumed that the formation of surface defective structures is related to the presence of SMSI.

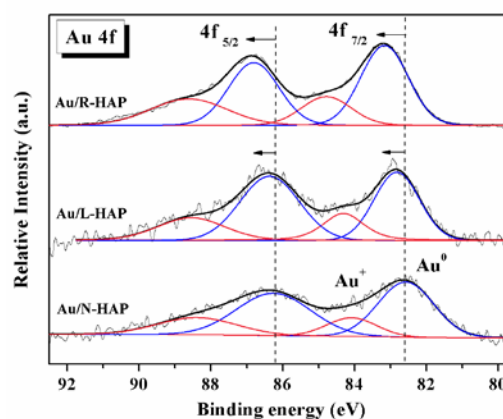


Figure 5. XPS of Au 4f regions for supported Au samples.

To investigate the electronic structures of Au species in samples, XPS of Au 4f region were examined. In the fine 4f spectra of Au species (Figure 5), there are two spin-orbit Au 4f 7/2 and Au 5/2 core levels at about 83.0 and 86.5 eV, respectively, indicative of the existence of metallic Au⁰ species. In comparison with that for bulk metallic Au⁰ (84.0 eV for Au 4f 7/2) reported in the literature, however, the binding energy (BE) value shifts to 82.6 eV for Au/N-HAP, 82.8 eV for Au/L-HAP and 83.2 eV for Au/R-HAP, respectively, indicative of the presence of the SMSI.^[51] Meanwhile, a second component at higher BE values of 84.1 eV for Au/N-HAP, 84.3 eV for Au/L-HAP and 84.8 eV for Au/R-HAP in the Au 4f 7/2 core level is associated with cationic Au⁺ species.^[52] Obviously, the relative proportion of Au⁺ in total Au species decreases gradually in the following order: Au/R-HAP > Au/L-HAP > Au/N-HAP (see Table 1), which suggests the enhanced metal-support interactions. As for Au/N-HAP, both a more negative shift of the BE value for Au 4f 7/2 of Au⁰ specie and a higher proportion of Au⁰ species in total Au species indicate a more intense electron transfer from the support to Au species, which results from a stronger interaction between Au species and the support, well consistent with the above Cs-STEM results.

As for supported catalysts, it is generally accepted that the high specific surface area of supports can greatly facilitate the dispersion of metal particles.^[53, 54] In our case, the BET specific

surface areas of Au/N-HAP and Au/L-HAP are approximately 6 and 4 times as that of Au/R-HAP (Table 1). Accordingly, the higher surface area of N-HAP support can mainly provide a beneficial dispersing effect for Au NPs, thus inhibiting the growth and agglomeration of Au species on the surface and resulting in the largest dispersion degree of Au species (Table 1), although Au NPs can be largely embedded into the N-HAP support stemming from SMSI. Thus, the average diameter of Au NPs on Au/N-HAP and Au/L-HAP is much smaller than that on the Au/R-HAP. As for Au/L-HAP sample, to a large extent, partially coated nanostructure of Au NPs hinders the exposure of Au species, although Au/L-HAP has higher surface area and smaller average size of Au NPs than Au/R-HAP. Therefore, the dispersion degree of Au species for Au/L-HAP is slightly larger than that for Au/R-HAP.

Surface acid-base properties of supported Au samples

Surface acid-base property of catalysts can play an important role in affecting the catalytic performance in many heterogeneous catalytic systems.^[55,56] As for amphoteric HAP support, surface acidic and basic sites are usually considered to be related to POH groups or metal ions and OH⁻ groups or O²⁻ ions of PO₄³⁻ groups, respectively.^[57,58]

In order to determine surface acidity, *in situ* FT-IR of pyridine adsorbed on supported Au samples were measured (Figure 6). In each case, a strong band at about 1454 cm⁻¹ is assigned to the vibration of pyridine adsorbed on Lewis acidic sites associated with metal Ca²⁺ ions,^[59-62] while a weak band at 1545 cm⁻¹ is assigned to the vibration mode of pyridine adsorbed on Brønsted acidic sites related to the POH group in the HAP structure.^[63] And, an observable small shoulder band at 1609 cm⁻¹ is probably associated with pyridine adsorbed on strong Lewis acidic sites.^[64] Meanwhile, four absorption bands for physisorbed (1439, 1565, 1580 cm⁻¹) and H-bonding adsorbed (1591 cm⁻¹) pyridine are observed in all samples.^[64] Specially, the enhancement in the relative intensity of absorption band at 1454 cm⁻¹ from Au/R-HAP to Au/L-HAP and Au/N-HAP clearly reveals the gradually increased amount of surface Lewis acidic sites.

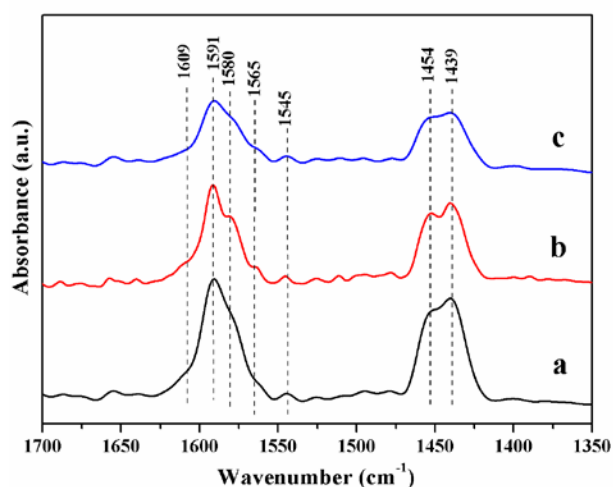


Figure 6. *In situ* FT-IR spectra of pyridine adsorbed on different samples: (a) Au/N-HAP, (b) Au/L-HAP and (c) Au/R-HAP.

NH₃-TPD also was examined to determine the strength and amount of surface acidic sites on samples. As shown in Figure 7, there are mainly three desorption ranges in the TPD profiles: the desorption below 250 °C is attributed to desorption of NH₃ from weak acidic sites; the second one at 250-400 °C is assigned to NH₃ desorption from medium-strength acidic site,^[65] the third one above 400-650 °C is ascribed to NH₃ desorption from strong acidic sites. Specially, Au/N-HAP also presents a small desorption in the range 650–800 °C, owing to desorption of NH₃ from super strong acidic sites. Such super strong acidic sites are probably related to the synergistic interaction between POH groups and metal Ca²⁺ ions in the structure of N-HAP support, as well as the high coordination number of metal Ca²⁺ ions. According to integral areas of desorption peaks, the amount of total acidic sites increases gradually from Au/R-HAP to Au/L-HAP and Au/N-HAP (Table 1), probably due to the lowering of the Ca/P molar ratio originating from the formation of more HPO₄²⁻ groups in the structure of HAP, as well as the increased specific surface area. Notably, the proportion of strong and super strong acidic sites in the total amount of acid sites increases gradually from 39 % for Au/R-HAP to 48 % for Au/L-HAP and 60 % for Au/N-HAP.

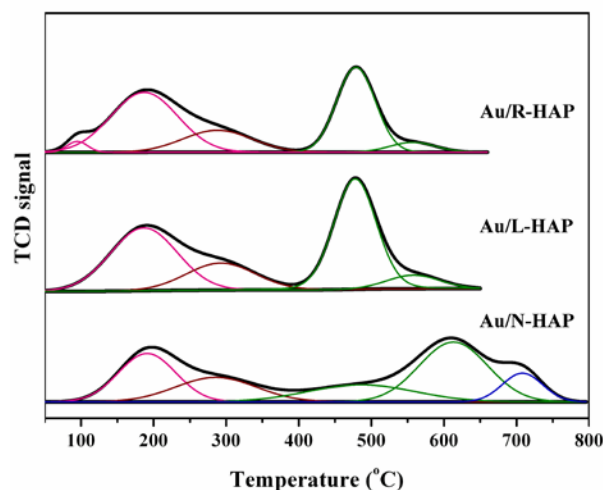


Figure 7. NH₃-TPD profiles of different supported Au samples.

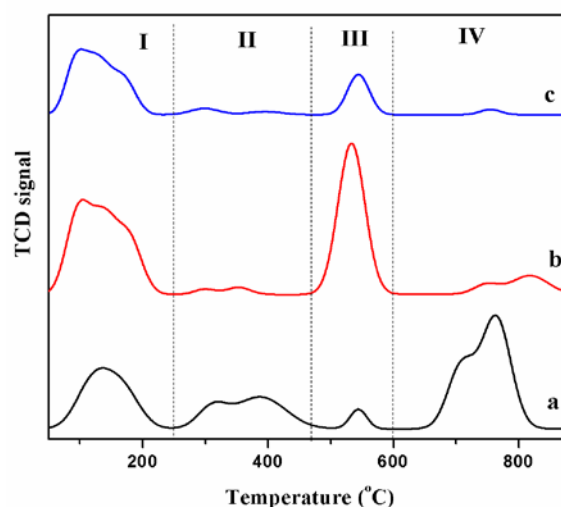
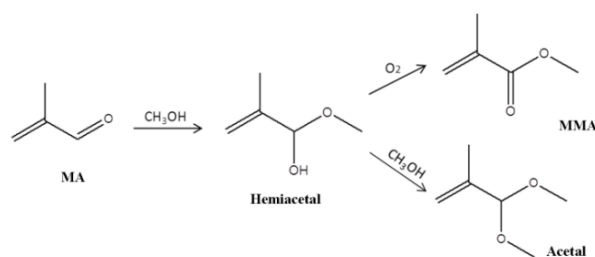


Figure 8. CO₂-TPD profiles of supported Au samples: (a) Au/N-HAP, (b) Au/L-HAP and (c) Au/R-HAP.

On the other side, to probe surface basicity of supported Au samples, CO₂-TPD was examined (Figure 8). Clearly, all of supported Au samples show four desorption ranges: the first desorption (I) below 250 °C is assigned to the CO₂ desorption from weak basic sites; the second desorption (II) at 250-470 °C to that from medium-strength basic sites; the third desorption (III) at 470-600 °C to that from strong basic sites; the fourth one (IV) above 600 °C to that from super strong basic sites.^[66,67] Among them, weak basic sites are related to hydrogenocarbonate species originating from surface hydroxyl groups, while medium-strength and strong basic sites are mainly related to surface carbonate coordinating with PO₄³⁻ (or HPO₄²⁻) groups and O²⁻ ions in the structure of HAP supports.^[63] Although the Ca/P molar ratio in samples is slightly lowered in the following order: Au/R-HAP > Au/L-HAP > Au/N-HAP, the amount of total basic sites shows a great increase. Specially, Au/N-HAP provides a much higher amount of strong and super strong basic sites (Table 1). The above results suggest that the great encapsulation of Au NPs by the N-HAP support, i.e., the formation of SMSI, probably leads to the formation of more and stronger basic sites on the surface, which is closely associated with the presence of more surface defects on the Au/N-HAP.

Catalytic performance of supported Au catalysts



Scheme 1. Main reaction pathways for the oxidative esterification of MA with methanol.

Scheme 1 shows possible main reaction pathways that happen in the course of oxidative esterification of MA with methanol. Generally, the first step is the condensation between MA and methanol to produce hemiacetal.^[9,13] Further, hemiacetal is oxidized to form MMA in the presence of molecular oxygen. Meanwhile, further condensation between hemiacetal and methanol can occur, and thus acetal by-product is generated.

The catalytic oxidative esterification of MA with methanol was conducted over different supported Au catalysts. Figure 9 shows MA conversion and MMA selectivity with the reaction time at 70 °C, and the results are summarized in Table 3 (GC-MS spectra of typical experiments are shown in Figures S1 and S2). Clearly, the structure of HAP supports exerts an important impact on the oxidative esterification of MA. Notably, Au/N-HAP generates a high MMA selectivity of ~98 % at 68 % conversion after reaction for 2.0 h. In this case, the MMA selectivity almost keeps unchanged within the whole reaction process. For Au/L-HAP and Au/R-HAP, however, the conversions only reach 48 % and 36 %, respectively, together with low MMA selectivities (76 % for Au/L-HAP and 43 % for Au/R-HAP). In two cases, more acetal by-product is generated. Noticeably, the TOF (turnover frequency) value for Au/N-HAP

(1792 h⁻¹) is about 2.2 times and 3.4 times as those for Au/L-HAP and Au/R-HAP, respectively, indicating a greatly enhanced catalytic activity. If the methanol/MA molar ratio is further increased from 8:1 to 40:1, a complete MMA conversion can be achieved over the Au/N-HAP after reaction for 2 h. In contrast, other single metal oxides (CaO, SiO₂, Al₂O₃, and MgO) supported Au reference catalysts with the similar metal loadings show greatly lowered catalytic activities with much lower conversions (Table 3), although relatively higher MMA selectivities are obtained over basic CaO and MgO supported catalysts in comparison with Au/L-HAP and Au/R-HAP.

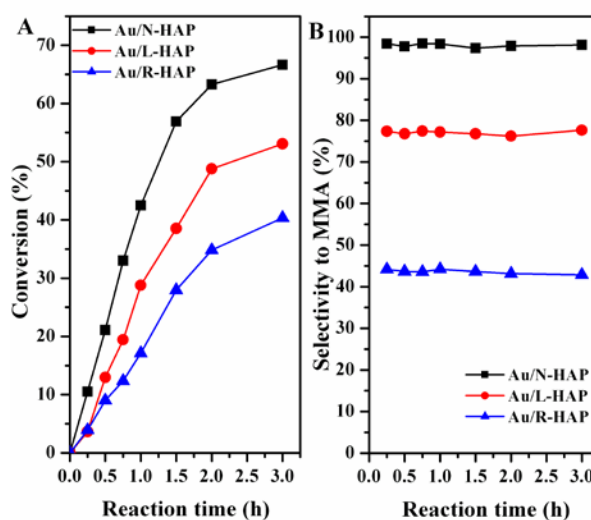


Figure 9 MA conversion (A) and MMA selectivity (B) with the reaction time over supported Au catalysts in the oxidative esterification of MA. Reaction conditions: methanol/MA molar ratio, 8:1; oxygen pressure, 0.1 MPa; reaction temperature, 70 °C.

Table 3 Catalytic oxidative esterification of MA over catalysts.^[a]

Catalyst	TOF ^[b] (h ⁻¹)	Conv. (%)	Selectivity (%)		
			MMA	Acetal	Others ^[c]
N-HAP ^[d]	--	38	2	97	1
Au/N-HAP	1792	68	98	0	2
Au/L-HAP	1101	48	76	18	6
Au/R-HAP	397	36	43	53	4
Au/N-HAP ^[e]	2501	87	99	0	1
Au/N-HAP ^[f]	2918	100	99	0	1
Au/N-HAP ^[g]	--	34	4	95	1
Au/CaO	29	13	90	3	7
Au/SiO ₂	6	5	47	35	18
Au/Al ₂ O ₃	3	25	6	85	9
Au/MgO	20	13	83	5	12

[a] Reaction conditions: methanol/MA molar ratio, 8:1; reaction temperature, 70 °C; oxygen pressure, 0.1 MPa; reaction time, 2 h. [b] TOF of MMA produced, which was given as the overall formation rate of MMA normalized by the number of active metallic Au sites within the initial 30 min. [c] By-products: isobutyric acid, methacrylic acid, and isobutyl aldehyde. [d] N₂ atmosphere. [e] Methanol/MA molar ratio, 20:1. [f] Methanol/MA molar ratio, 40:1. [g] N₂ atmosphere.

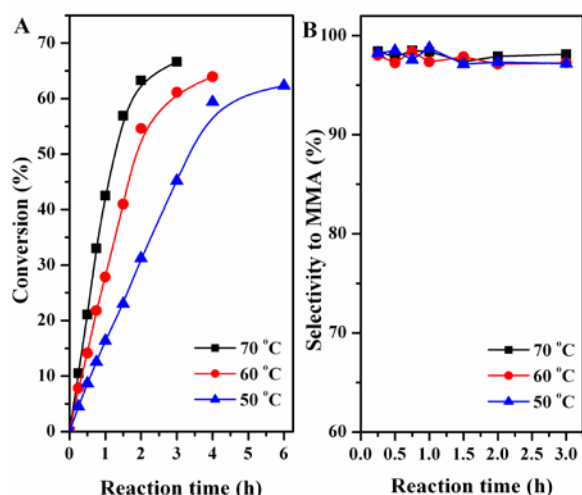


Figure 10 Effect of the reaction temperature on the MA conversion (A) and the MMA selectivity (B) over the Au/N-HAP with the reaction time. Conditions: methanol/MA molar ratio, 8:1; oxygen pressure, 0.1 MPa.

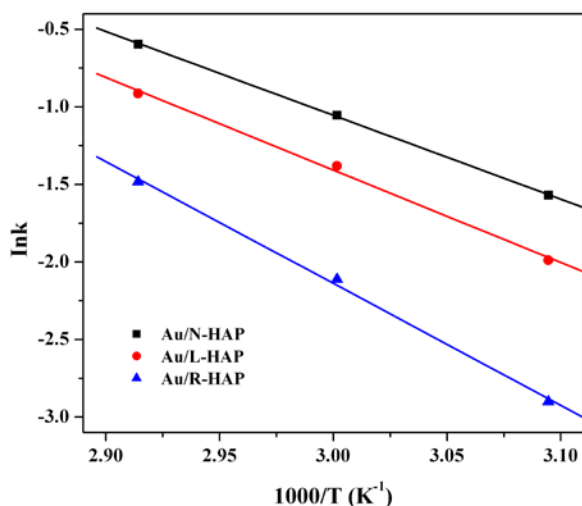


Figure 11 $\ln(\text{reaction rate constant})$ vs. reciprocal of reaction temperature over different supported Au catalysts in the oxidative esterification of MA.

As shown in Figure 10, the reaction temperature has a significant effect on the MA conversion over the Au/N-HAP. When the reaction temperature is elevated from 50 to 70 °C, the MA conversion is significantly increased due to the enhanced reaction rate, as well as the nature of endothermic reaction. No obvious change in the MMA selectivity with the reaction temperature is observed. Based on the MMA conversions over different HAP supported Au catalysts at different temperatures (Figure S3), one can note that $-\ln(1-x)$ (x : MA conversion) linearly increases with the reaction time

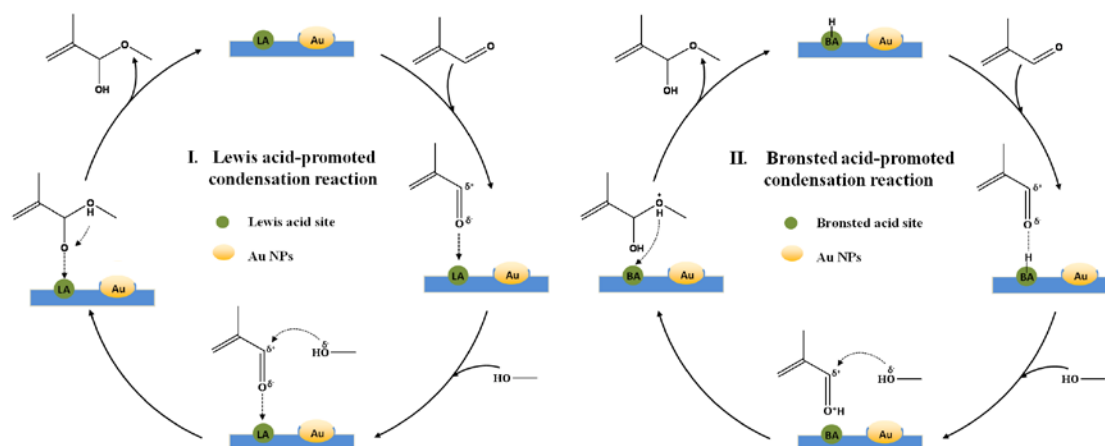
(Figure S4), demonstrating that the oxidative esterification of MA obeys first-order kinetics in the presence of excess methanol. According to the linear relationship between $\ln k$ (k : reaction rate constant) and reaction temperature (Figure 11), the apparent activation energy of the oxidative esterification of MA determined from Arrhenius equations is about 45 kJ/mol for Au/N-HAP, 50 kJ/mol for Au/L-HAP and 65 kJ/mol for Au/R-HAP, respectively. The aforementioned results further confirm the excellent catalytic performance of Au/N-HAP catalyst.

In order to investigate the reusability of as-synthesized supported Au/N-HAP catalyst, the spent catalyst was collected and washed with ethanol and deionized water for several times, dried overnight, and reused in next cycling tests. As shown in Figure S5, after recycling for four times, the MMA conversion only reduced slightly from 68 % to 64 %. Meanwhile, there is no observable change in the MMA selectivity. Further, elemental ICP-AES analysis shows that the weight loss of Au is only about 0.86 wt % in the total Au content in the Au/N-HAP after four cycles. The above results demonstrate the high stability of the present Au/N-HAP catalyst, due to the presence of SMSI.

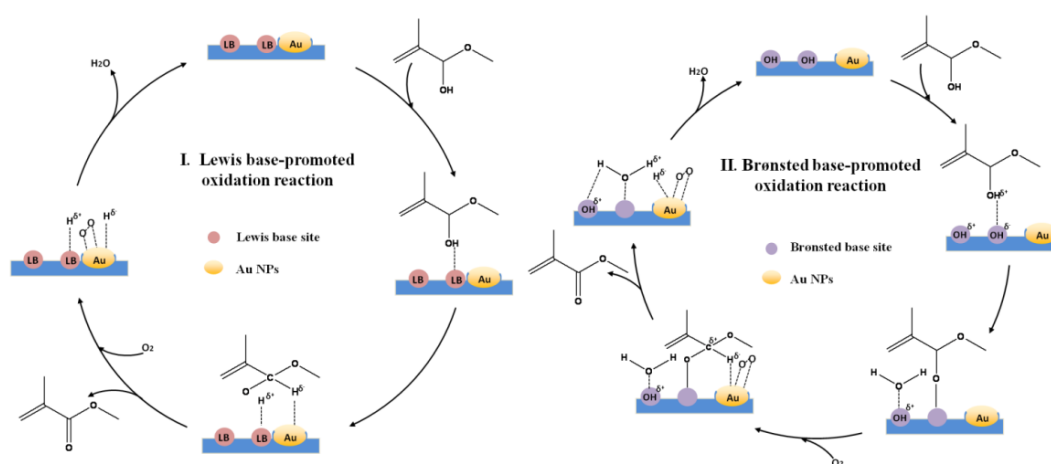
Reaction mechanism for oxidative esterification of MA

Previously, it was reported that surface acidic sites on catalysts facilitated the oxidative transformation of aldehydes and the further formation of acetals in the course of oxidative esterification of benzaldehyde with methanol.^[11] In our case, compared with other two supported catalysts, Au/N-HAP with relatively more surface strong acidic sites shows better catalytic performance with much higher MMA selectivity and MA conversion. In addition, under inert N_2 atmosphere, pure N-HAP support and Au/N-HAP catalyst also are found to exhibit moderate conversions of MA with high selectivities to acetal by-product (>95 %) (Table 3). It demonstrates that surface acidity should play an important role in controlling the condensations between MA (or hemiacetal) and methanol.

Based on the above characterizations and catalytic tests, we tentatively propose Lewis-acid (I) and Brønsted acid (II) jointly promoted mechanism of the condensation between MA and methanol on the Au/N-HAP (Scheme 2). On the hand, surface Lewis acidic sites as electrophilic centers or electron acceptors can facilitate the activation of the C=O bond in MA via its lone electron pair in oxygen,^[68-71] thereby leading to the condensation by direct nucleophilic attack of methanol to the carbonyl group in MA and the following formation of hemiacetal intermediate. On the other side, the proton from Brønsted acid sites on the support also can interact with MA through coordinating with the oxygen atom of carbonyl group to weaken the C=O bond, thus forming protonated MA. Subsequently, the electrophilic carbon of carbonyl group in protonated MA is susceptible to be attacked by nucleophilic methanol species, which can greatly promote the occurrence of the condensation between MA and methanol. At last, hemiacetal intermediate is formed.



Scheme 2. Proposed Lewis acid (I) and Brønsted acid (II) jointly promoted mechanism of the condensation between MA and methanol over Au/N-HAP.



Scheme 3. Proposed Lewis base (I) and Brønsted base (II) jointly promoted mechanism of hemiacetal oxidation over Au/N-HAP.

Further, hemiacetal intermediate can be oxidized to produce MMA product in the presence of active Au NPs and molecular oxygen. Herein, surface basic sites can play an important role in controlling the hemiacetal oxidation. A possible mechanism of hemiacetal oxidation over the Au/N-HAP promoted by surface cooperative effect between Lewis/Brønsted basic sites and active Au species also is proposed (Scheme 3). First, hydroxyl group in hemiacetal can interact with Lewis basic sites adjacent to active metallic Au sites. Then, the hydrogen in hydroxyl group is abstracted to the support and the resulting negatively charged alkoxide intermediate coordinates with active Au species at the interface. Subsequently, unsteady β -hydride formed through the metal-H bond is eliminated to generate a metal-hydride species,^[72] while MMA product is produced. Finally, molecular oxygen is activated by metallic Au species through a double linear model,^[73,74] and thus both adsorbed proton and metal-hydride on the surface are oxidized at the metal-support interface to generate water. Meanwhile, Brønsted basic sites can uniquely activate the hydroxyl group of hemiacetal to promote the formation of metal alkoxide. That is, hydroxyl hydrogen in hemiacetal interacts with Brønsted base (OH), resulting in the formation of alkoxide intermediate at the interface and water molecule located at the other Brønsted base site. Similarly, the β -H atom in alkoxide coordinating with Au species also

undergoes the β -hydride elimination to form metal-hydride species at the catalyst interface and MMA product. At last, activated oxygen in the form of Au-O-O-Au species on the surface rapidly reacts with the metal-hydride and hydrogen atom in adsorbed water molecule, while original Brønsted basic sites are recovered to finish the catalytic oxidation process. Accordingly, in the absence of strong basic sites, further condensation between hemiacetal and methanol easily take place and thus more acetal by-product is formed in the cases of Au/L-HAP and Au/R-HAP, as evidenced by the experimental results.

Among three supported catalysts, Au/N-HAP possesses the largest amounts of surface acidic and basic sites, which greatly promote the chemisorption-activation of MA and reaction intermediate molecules. Meanwhile, Au/N-HAP catalyst provides the most amounts of catalytically active Au⁰ sites on the surface due to the highest dispersive nature of Au species, which plays a crucial factor for facilitating the formation of β -hydride and the oxygen activation in the course of the oxidation of hemiacetal. Accordingly, Au/N-HAP constructs the strongest cooperative effect between Au species and surface acid-base sites, thus resulting in the superior catalytic performance. As a result, compared with Au/L-HAP and Au/R-HAP, Au/N-HAP catalyst exhibits much higher catalytic performance.

Conclusions

In summary, three types of needle-like, lamella-like and rod-like HAPs supported Au catalysts are successfully synthesized. A series of characterizations including XRD, SEM, TEM, Cs-STEM, XPS, in situ FT-IR adsorption, TPD results demonstrate the formation of well-dispersed Au⁰ NPs and surface defects on catalysts. Surface defects on catalysts caused by the encapsulation of Au NPs by HAP supports are found to be helpful to the generation of strong basic sites. Compared with other HAP supported ones, needle-like HAP supported catalyst shows much better catalytic performance in terms of both the activity and the MMA selectivity under mild reaction conditions. It is believed that the cooperation between surface acid-base sites and highly dispersive active Au species constitutes an efficient catalytic reaction environment, thus being beneficial to the chemisorption of MA, and the formation of β -hydride and the following oxygen activation in the oxidative esterification of MA. The present work develops new high-performance supported Au catalysts with abundant surface acid-base sites for practical industrial production of MMA by one-step direct oxidative esterification of MA under mild reaction conditions.

Experimental Section

Synthesis of HAP supports and supported catalysts

Synthesis of needle-like HAP. Calcium oxide (0.28 g) was added into 100 mL of distilled water under vigorous stirring at nitrogen atmosphere for 30 min to obtain Ca(OH)₂ suspension. Subsequently, a solution of Na₃PO₄·12H₂O (1.14 g) dissolved in 20 mL of distilled water was slowly added into the above suspension, and continuously stirred for 2 h under ultrasonic condition. The resultant suspension was filtered, and the obtained solid was dried at 70 °C overnight and then calcined at 400°C for 4h at a ramping rate of 2°C/min at air. The obtained HAP was labeled as N-HAP.

Synthesis of lamella-like HAP. Calcium oxide (0.28 g) and NH₄H₂PO₄ (0.35 g) were dissolved in a mixture solvent of N,N-dimethylformamide (DMF, 25mL) and deionized water (10 mL). The solution obtained was aged at 120°C for 24 h. Subsequently, the resultant suspension was filtered. At last, the obtained solid was dried and calcined according to the identical procedure to N-HAP. The obtained HPA was labeled as L-HAP.

Synthesis of rod-like HAP. The synthesis procedure was similar with that of L-HAP, except that the solvent was replaced by a pure DMF (35 mL). The obtained HAP was labeled as R-HAP.

Synthesis of supported Au catalysts. Supported Au catalysts were synthesized by a urea homogeneous deposition-precipitation method. Typically, polyvinylpyrrolidone (PVP, 0.3 g) was dispersed in 100 mL of deionized water with stirring. Then, 2.1 mL of HAuCl₄ solution (24.28 M) was added into the above solution under stirring for 30 min. Afterwards, HAP support (0.5g) was added into HAuCl₄ solution and stirred for 30 min. Then, a urea solution (0.1 M) was added into the above suspension until pH = 9.0. Subsequently, the suspension was aged at 60°C for 1 h. Finally, the white precipitate was filtered, washed with deionized water for several times until pH was 7, dried at 70°C overnight and reduced at 300 °C (2°C/min) for 2 h in a muffle furnace at air.

Characterization

X-ray diffraction (XRD) experiments were carried out on Shimadzu XRD-6000 powder diffraction spectrometer with

graphite-filtered Cu-K α source ($\lambda = 0.15418$ nm) as the X-ray source and the scanning rate of 10°/min.

Elemental analysis of samples was performed by using a Shimadzu ICPS-7500 inductively coupled plasma atomic emission spectroscopy (ICP-AES). The sample was dissolved by aqua regia before measurements.

Low temperature nitrogen adsorption-desorption experiments were performed on Micromeritics ASAP 2020 sorptometer apparatus at -196 °C. The Brunauer–Emmett–Teller (BET) method was used to calculated specific surface areas.

Transmission electron microscopy (TEM) and high resolution transmission electron microscopy (HRTEM) tests were conducted using a JEOL 2100 electron microscope with the accelerating voltage of 80–200 kV. Spherical aberration corrected scanning transmission electron microscope (Cs-STEM) images was recorded using a Cs-corrected JEOL JEM-ARM200F instrument.

Positron annihilation spectroscopy (PAS) was characterized by a fast/slow coincidence ORTEC system using ²²Na as radioactive positron source (13×10^{-6} Ci) with a time resolution of 210 ps full width at half maximum in the transmission mode at the Beijing Synchrotron Radiation Facility (BSRF).

CO pulse chemisorption of samples was carried out on a Micromeritics AutoChem II 2920 instrument with a thermal conductivity detector (TCD). The sample (0.1 g) was heated to 200 °C under He flow (40 ml/min) and then held for 1h. After the temperature was reduced to 50 °C, pure CO gas was fed according to a pulse titration procedure until the signal peak area was constant. The dispersion of Au was determined based on the CO/Au adsorption ratio of 1:1.

X-ray photoelectron spectroscopy (XPS) experiments were performed on VG ESCALAB 250 electron spectrometer at the vacuum degree of 2×10^{-9} Pa. The Al K α ($h\nu = 1486.6$ eV) was used as the target source. Binding energies were calibrated using C1s peak at 284.6 eV.

In situ Fourier transform infrared (FT-IR) of pyridine adsorption test was performed on a Nicolet 380 type spectrophotometer. First, the sample (40 mg) were pressed into a thin slice and put into the in situ IR cell. Then in N₂ atmosphere, the sample was heated to 200 °C and held for 1h. When the temperature of the cell was reduced to 25 °C, pyridine was introduced and balanced at this temperature for 2 h. FT-IR spectra were recorded under vacuum conditions.

Temperature-programmed desorption was tested using Chemisorb 2720 instrument with a TCD. The sample (0.1g) was first heated to 200 °C in a He flow (40 ml/min) and held for 1 h. After the temperature was cooled down to 50 °C, the sample tube was put into pure NH₃ (or CO₂) for 1h, and purged with a He flow for 1 h. Finally, the temperature was increased to 700 °C at a rising rate of 5 °C/min.

Catalytic test

The catalytic oxidative esterification of MA was carried out in a 50 mL glass reactor with a magnetic stirrer, where the catalyst (0.1 g), MA (1.04 ml) and methanol (4 ml) were charged. Before reaction, the reactor was purged with ultrahigh purity O₂ flow (30 ml/min) for three times, and each time was held for 2 min. Then, the temperature of the reactor was increased to 70 °C. Subsequently, the O₂ was fed into the reactor and the relative pressure was kept at 0.1 MPa. At last, the reaction was performed with a stirring speed of 1000 rpm. A schematic diagram of a reaction apparatus is presented at supporting information (Scheme S1). After 2h, the reactor was cooled in an ice bath, and the

reactants were centrifuged and quantitatively analyzed by gas chromatography (GC) using an Agilent GC7890B equipped with DB-WAX capillary polarity chromatographic column (30.0 m×320 mm×0.25 mm) and hydrogen flame ionization detector. Further, the liquid products were determined by GC-MS using a Shimadzu QP 2010 equipped with a DB-5 column. The conversions and selectivities of products were calculated according to the internal standard method using cyclohexane as standard substance. In all cases, the carbon balances were above 97 %. The spent solid catalyst was washed with acetone and deionized water. After drying at 70 °C overnight, the catalyst was reused for evaluating reusable performance.

Acknowledgment

We gratefully thank the financial support from National Natural Science Foundation of China (21325624; 21521005) and the Fundamental Research Funds for the Central Universities (buctrc201528).

Keywords: Oxidative esterification • Methyl methacrylate • Acid-base sites • Hydroxyapatite • Gold.

References

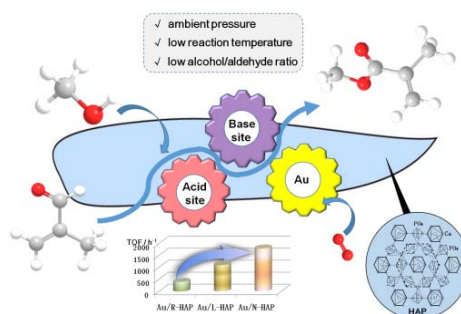
- [1] E.N. Marvell, M. J. Joncich, *J. Am. Chem. Soc.* **1951**, *73*, 973–975.
- [2] E.J. Corey, N.W. Gilman, B.E. Ganem, *J. Am. Chem. Soc.* **1968**, *90*, 5616–5617.
- [3] J.J. Spivey, M.R. Gogate, J.R. Zoeller, R.D. Colberg, *Ind. Eng. Chem. Res.* **1997**, *36*, 4600–4608.
- [4] K. Nagai, *Appl. Catal. A* **2001**, *221*, 367–377.
- [5] J. Andraos, *ACS Sustainable Chem. Eng.* **2016**, *4*, 312–323.
- [6] D.I. Enache, J.K. Edwards, P. Landon, B. Solsona-Espriu, A.F. Carley, A.A. Herzing, M. Watanabe, C.J. Kiely, D.W. Knight, G.J. Hutchings, *Science* **2006**, *311*, 362–365.
- [7] J. Lichtenberger, D. Lee, E. Iglesia, *Phys. Chem. Chem. Phys.* **2007**, *9*, 4902–4906.
- [8] C. Liu, J. Wang, L. Meng, Y. Deng, Y. Li, A. Lei, *Angew. Chem. Int. Ed.* **2011**, *50*, 5144–5148.
- [9] Y. Diao, R. Yan, S. Zhang, P. Yang, Z. Li, L. Wang, H. Dong, *J. Mol. Catal. A* **2009**, *303*, 35–42.
- [10] Y. Li, L. Wang, R. Yan, J. Han, S. Zhang, *Catal. Sci. Technol.* **2016**, *6*, 5453–5463.
- [11] F.-Z. Su, J. Ni, H. Sun, Y. Cao, H.-Y. He, K.-N. Fan, *Chem.–Eur. J.* **2008**, *14*, 7131–7135.
- [12] X. Wan, W. Deng, Q. Zhang, Y. Wang, *Catal. Today* **2014**, *233*, 147–154.
- [13] K. Suzuki, T. Yamaguchi, K. Matsushita, C. Iitsuka, J. Miura, T. Akaogi, H. Ishida, *ACS Catal.* **2013**, *3*, 1845–1849.
- [14] J.A. Lopez-Sanchez, N. Dimitratos, C. Hammond, G.L. Brett, L. Kesavan, S. White, P. Miedziak, R. Tiruvalam, R.L. Jenkins, A.F. Carley, D. Knight, C.J. Kiely, G.J. Hutchings, *Nat. Chem.* **2011**, *3*, 551–556.
- [15] K. Zhao, H. Tang, B. Qiao, L. Li, J. Wang, *ACS Catal.* **2015**, *5*, 3528–3539.
- [16] C.W. Corti, R.J. Holliday, D.T. Thompson, *Top. Catal.* **2007**, *44*, 331–343.
- [17] W. Yan, S.M. Mahurin, Z. Pan, S.H. Overbury, S. Dai, *J. Am. Chem. Soc.* **2005**, *127*, 10480–10481.
- [18] K. Zhao, B. Qiao, J. Wang, Y. Zhang, T. Zhang, *Chem. Commun.* **2011**, *47*, 1779–1781.
- [19] J. Wang, A.H. Lu, M. Li, W. Zhang, Y.S. Chen, D.X. Tian, W.C. Li, *ACS Nano* **2013**, *7*, 4902–4910.
- [20] P. N. Amaniampong, K. Li, X. Jia, B. Wang, A. Borgna, Y. Yang *ChemCatChem* **2014**, *6*, 2105–2114.
- [21] G.L. Haller, D.E. Resasco, *Adv. Catal.* **1989**, *36*, 173–235.
- [22] A.D. Logan, E.J. Braunschweig, A.K. Datye, *Langmuir* **1988**, *4*, 827–830.
- [23] E.J. Braunschweig, A.D. Logan, A.K. Datye, D.J. Smith, *J. Catal.* **1989**, *118*, 227–237.
- [24] H. Tang, J. Wei, F. Liu, B. Qiao, X. Pan, L. Li, J. Wang, T. Zhang, *J. Am. Chem. Soc.* **2016**, *138*, 56–59.
- [25] J.C. Elliott, *Structure and Chemistry of the Apatites and Other Calcium Orthophosphates*, Elsevier, **2011**, pp1–61, 111–190.
- [26] K. Mori, K. Yamaguchi, T. Hara, T. Mizugaki, K. Ebitani, K. Kaneda, *J. Am. Chem. Soc.* **2002**, *124*, 11572–11573.
- [27] K. Kaneda, T. Mizugaki, *Energy Environ. Sci.* **2009**, *2*, 655–673.
- [28] H. Sun, F. Z. Su, J. Ni, Y. Cao, H. Y. He, K. N. Fan, *Angew. Chem. Int. Ed.* **2009**, *48*, 4390–4393.
- [29] B. Yan, L. Z. Tao, Y. Liang, B. Q. Xu, *ACS Catal.* **2014**, *4*, 1931–1943.
- [30] M. Zahmakiran, Y. Tonbul, S. Özkar, *Chem. Commun.* **2010**, *46*, 4788–4790.
- [31] M. Zahmakiran, Y. Roman-Leshkov, Y. Zhang, *Langmuir* **2012**, *28*, 60–64.
- [32] P. Zhang, T. B. Wu, T. Jiang, W. T. Wang, H. Z. Liu, H. L. Fan, Z. F. Zhang, B. X. Han, *Green Chem.* **2013**, *15*, 152–159.
- [33] G. Xu, J. Guo, Y. Zhang, Y. Fu, J. Chen, L. Ma, Q. Guo, *ChemCatChem* **2015**, *7*, 2485–2492.
- [34] K. Mori, M. Oshiba, T. Hara, T. Mizugaki, K. Ebitani, K. Kaneda, *New J. Chem.* **2006**, *30*, 44–52.
- [35] S. Mallouk, K. Bougrin, A. Laghizil and R. Benhida, *Molecules* **2010**, *15*, 813–823.
- [36] M. Gruselle, T. Kanger, R. Thouvenot, A. Flambard, K. Kriis, V. Mikli, R. Traksmaa, B. Maaten, K. Tonsuaada, *ACS Catal.* **2011**, *1*, 1729–1733.
- [37] S. Ogo, A. Onda, Y. K, *Catalysts. Appl. Catal. A* **2011**, *402*, 188–195.
- [38] T. Tsuchida, S. Sakuma, T. Takeguchi, W. Ueda, *Ind. Eng. Chem. Res.* **2006**, *45*, 8634–8642.
- [39] T. Tsuchida, T. Yoshioka, S. Sakuma, T. Takeguchi, W. Ueda, *Ind. Eng. Chem. Res.* **2008**, *47*, 1443–1452.
- [40] T. Tsuchida, J. Kubo, T. Yoshioka, S. Sakuma, T. Takeguchi, W. Ueda, *J. Catal.* **2008**, *259*, 183–189.
- [41] H. Nora, D. Leeuw, *J. Phys. Chem. B* **2004**, *108*, 1809–1811.
- [42] H. Ito, Y. Oaki, H. Imai, *Cryst. Growth Des.* **2008**, *8*, 1055–1059.
- [43] S. He, C. Li, H. Chen, D. Su, B. Zhang, X. Cao, B. Wang, M. Wei, D.G. Evans, X. Duan, *Chem. Mater.* **2013**, *25*, 1040–1046.
- [44] P.A. Kumar, M. Alatalo, V.J. Ghosh, A.C. Kruseman, B.K. Nielsen, G. Lynn, *Phys. Rev. Lett.* **1996**, *77*, 2097–2100.
- [45] V.P. Shantarovich, T. Suzuki, Y. Ito, K. Kondo, V.W. Gustov, I.V. Melikhov, S.S. Berdonosov, L.N. Ivanovc, R.S. Yu, *Radiat. Phys. Chem.* **2007**, *76*, 257–262.
- [46] J. Kanzy, T. Suzuki, *Radiat. Phys. Chem.* **2003**, *68*, 497–500.
- [47] M. Kong, Y. Li, X. Chen, T. Tian, P. Fang, F. Zheng, X. Zhao, *J. Am. Chem. Soc.* **2011**, *133*, 16414–16417.
- [48] D. Sanyal, D. Banerjee, U. De, *Phys. Rev. B* **1998**, *58*, 15226.
- [49] G. Ouyang, W.G. Zhu, G.W. Yang, Z.M. Zhu, *J. Phys. Chem. C* **2010**, *114*, 4929–4933.
- [50] W. Sun, Y. Li, W.Q. Shi, X.J. Zhao, P.F. Fang, *J. Mater. Chem.* **2011**, *21*, 9263–9270.
- [51] S. Wang, S.T. Yin, G.W. Chen, L. Li, H. Zhang, *Catal. Sci. Technol.* **2016**, *6*, 4090–4104.
- [52] K. Qian, W. Huang, J. Fang, S. Lv, B. He, Z. Jiang, S. Wei, *J. Catal.* **2008**, *255*, 269–278.
- [53] S. Wang, G. Sun, Z. Wu, Q. Xin, *J. Power Sources* **2007**, *165*, 128–133.
- [54] C. Wen, A. Yin, Y. Cui, X. Yang, W. Dai, K. Fan, *Appl. Catal. A* **2013**, *458*, 82–89.
- [55] J. T. Kozlowski, M. Behrens, R. Schlögl, R. J. Davis, *ChemCatChem* **2013**, *5*, 1989–1997.
- [56] R. Goyal, B. Sarkar, N. Lucus, A. Bordoloi, *ChemCatChem* **2014**, *6*, 3091–3095.
- [57] V.D.B.C. Dasireddy, S. Singh, H.B. Friedrich, *Appl. Catal. A* **2013**, *456*, 105–117.
- [58] D. Laurencin, N. Almora-Barrios, N.H. deleeuw, C. Gervais, C. Bonhomme, F. Mauri, W. Chrzanowski, J.C. Knowles, R.J.

- Newport, A. Wong, Z. Gan, M.E. Smith, *Biomaterials* **2011**, *32*, 1826–1837.
- [59] B. Tang, W. Dai, G. Wu, N. Guan, L. Li, M. Hunger, *ACS Catal.* **2014**, *4*, 2801–2810.
- [60] Q. Guo, F. Fan, E.A. Pidko, W.N.P. van der Graaff, Z. Feng, C. Li, E.J.M. Hensen, *ChemSusChem* **2013**, *6*, 1352–1356.
- [61] G. Busca, *Phys. Chem. Chem. Phys.* **1999**, *1*, 723–736.
- [62] H.Q. Wang, S. Gao, F.X. Yu, Y. Liu, X.L. Weng, Z.B. Wu, *J. Phys. Chem. C* **2015**, *119*, 15077–15084.
- [63] S. Diallo-Garcia, M.B. Osman, J. Krafft, S. Casale, C. Thomas, J. Kubo, G. Costentin, *J. Phys. Chem. C* **2014**, *118*, 12744–12757.
- [64] C.E. Volckmar, M. Bron, U. Bentrup, A. Martin, P. Claus, *J. Catal.* **2009**, *261*, 1–8.
- [65] J. Zuo, Z. Chen, F. Wang, Y. Yu, L. Wang, X. Li, *Ind. Eng. Chem. Res.* **2014**, *53*, 2647–2655.
- [66] L. Jia, J. Gao, W. Fang, *Catal. Commun.* **2009**, *10*, 2000–2003.
- [67] A. Azzouz, D. Nistor, D. Miron, *Thermochim Acta* **2006**, *449*, 27–34.
- [68] N. Asao, T. Nogami, K. Takahashi, Y. Yamamoto, *J. Am. Chem. Soc.* **2002**, *124*, 764–765.
- [69] F. Ammari, J. Lamotte, R. Touroude, *J. Catal.* **2004**, *221*, 32–42.
- [70] J. Gong, H. Yue, Y. Zhao, S. Zhao, L. Zhao, J. Lv, S. Wang, X. Ma, *J. Am. Chem. Soc.* **2012**, *134*, 13922–13925.
- [71] V. Gutierrez, M. Dennehy, A. Diez, M. Volpe, *Appl. Catal. A* **2012**, *437*, 72–78.
- [72] M. Conte, H. Miyamura, S. Kobayashi, V. Chechik, *J. Am. Chem. Soc.* **2009**, *131*, 7189–7196.
- [73] S. Nishimura, Y. Yakita, M. Katayama, K. Higashimine, K. Ebitani, *Catal. Sci. Technol.* **2013**, *3*, 351–359.
- [74] K. J. Sun, M. Kohyama, S. Tanaka, S. Takeda, *ChemCatChem* **2013**, *5*, 2217–2222.

Entry for the Table of Contents

FULL PAPER

Three needle-like, lamella-like, and rod-like hydroxyapatite supported gold nanocatalysts were employed in direct oxidative esterification of methacrolein to produce methyl methacrylate. Supported Au nanocatalyst over the needle-like hydroxyapatite presented a greatly enhanced catalytic performance, due to surface cooperative effect between abundant acid-base sites for preferential chemisorption of methacrolein and highly dispersed active Au species for the favourable formation of β -hydride and oxygen activation.



Jun Gao, Guoli Fan, Lan Yang, Xinzhong Cao, Peng Zhang, Feng Li*

Page No. – Page No.

Oxidative esterification of methacrolein to methyl methacrylate over gold nanoparticles on hydroxyapatite

Accepted Manuscript